Electrochemical Reduction of Carbon Dioxide to Methanol on Defective Graphene Supported Cu Based Single-Atom Catalysts: A First Principles Approach

jing liu
Tianjin University, Ministry of Education
jun zhao (zhaojun@tju.edu.cn)
Tianjin University, Ministry of Education
yang li
Tianjin University, Ministry of Education
chuangwei liu
Technical University of Denmark
Mohamed E Zayed
Tianjin University, Ministry of Education

Research Article

Keywords: CO2 reduction reaction (CO2RR), Methanol, Density functional theory, Single-atom-copper catalyst, Three coordinated single-copper atom (Cu-G3), four coordinated single- copper atom (Cu-G4)

Posted Date: August 29th, 2022

DOI: https://doi.org/10.21203/rs.3.rs-1990072/v1

Abstract

Electrochemical CO_2 reduction reaction to clean fuels is recently regarded as one of the most promising routes to meet the global demand for energy and environmental riskiness. In this work, we explored and compared the mechanism of electrochemical reduction of CO_2 to methanol by graphene (G)-supported single-atom-copper (Cu) catalysts. The free energies of the CO2 reduction intermediates in electrochemical reaction pathways were calculated by using density functional theory coupled with a computational hydrogen electrode approach. Moreover, the physical and electronic characteristics of the two catalysts were examined via binding energy, atomic distance, bader charge, band structure, and density of states calculations. The computational results show that the three coordinated single-copper atom (Cu-G3) is slightly oxidized, whereas the four coordinated single-copper atom (Cu-G4) is heavily oxidized. In particular, the Cu-G3 is the more suitable catalytic for the conversion of CO2 to CH3OH. Moreover, two various pathways (*HCOO and *COOH) on the two proposed catalysts (Cu-G3 and Cu-G4) are explored based on the initially produced intermediates. The Cu-G3/G4 catalysts robustly promote the HCOO* pathway with an energy barrier of 0.41 eV (*HCOOH → *CHO) and 0.50 eV (*CO_2 → *HCOO). However, the rate-limiting step for the *COOH pathway on Cu-G3/G4 catalysts is (*CO → *CHO), with limiting potentials of 1.1 eV and 1.13 eV, respectively. Hence, the reduction of CO2 to methanol on graphene supported single-atom-copper highly prefers to *HCOO pathway. Lastly, we focus on the mechanism of the rate-limiting step (*CO → *CHO). The linear relationship between *CO and *CHO binding energy is broken by the single Cu atom. And the s-p electrons of copper have filled the antibonding orbital of Cu-G4 and weakened the binding with CHO, resulting in a slightly higher energy barrier for the Cu-G4 than Cu-G3. Conclusively, the current study provides a reference for non-noble metal monatomic catalysis of carbon dioxide to methanol with optimal product selectivity.

1. Introduction

Fossil fuels combustion for different human activities, including transportation, industrial manufacturing, electricity production, and heat energy consumption, is regarded as the most effectual parameter in CO_2 emissions. CO_2 gas is a crucial source of greenhouse gases, and the enormous CO_2 pollutants have been associated with the world, global warming and deterioration of living environment. The CO2 reduction reaction (CO2RR) to clean fuels has been recently considered as one of the most promising utilization method to meet the global energy demand and mitigate the CO_2 greenhouse effect, which has drawn ever-growing attention [1–2]. With regard to CO2 conversion, various kind of control strategy have been published, including chemical methods, photochemical methods, and electrochemical methods, which involve diversified products from CO_2 reduction are HCOOH, HCHO, C_2H_5OH, CH_4, CH_3OH, etc., depending on the number of transferred electrons [3–4]. The electrochemical method is one of the most promising ways of CO2 conversion [5]. It is the most straight forward approach, the way has attracted more and more interest in industrial circles and scientific community, and it is also expected to use renewable electricity from solar energy [6].

However, the high critical potential and low selectivity of catalysts are the two bottlenecks in CO2 convert to other chemicals and both of them are strongly dependent on electrode materials [7–8]. Because the d-band of transition metals is close to the Fermi level, it can overcome the inherent activation barrier and reaction kinetics, so this kind of transition metals is particularly attractive [9–10]. We also observed a linear constraint relationship between the adsorption/desorption, activity, and selectivity of transition metal bulk catalysts, however, the research shows that single-atom catalysts can break this relationship [11]. In fact, a large number of studies have shown that transition metal based catalysts such as copper, iron, nickel, gold, platinum and palladium have been used to improve the energy efficiency of electrochemical reduction of CO_2 to produce economically valuable small molecular products [12]. Among them, copper (Cu) is widely considered as a great future metal for CO2 reduction because of its ability to produce hydrocarbon fuels such as methane (CH4), formic acid (HCOOH), and methanol (CH3OH). Also, graphene, a monolayer of graphite, has attracted of a large number of researchers at home and abroad since its discovery [13–14]. Monatomic copper supported by defective graphene shows many valuable physical and chemical phenomena due to its special two-dimensional material structure. The choice of this underlying substrate is because of its common use in experiments [15]. Furthermore, changes atomic vacancy number of graphene may help to break the stability and improve the surface activity of copper for absorbing more CO_2. Also, the band structure of graphene will change in varying degrees due to the defect density, then it affects the physicochemical properties and magnetism of the catalyst. [16–17].

Recently, single-atom catalysts (SACs) have attracted more and more attention and research in catalytic reactions. Single-atom catalysis is different from nanocatalysis. When the dispersion of metal particles reaches the single-atom level, the free energy of the metal surface increases sharply, which has a quantum size effect. This will affect the reaction kinetics and improve the utilization efficiency of metal atoms [18]. SACs were firstly defined by Yang et al and Qiao et al [19–20]. Subsequently, various seed capsules for fixing metal atoms at the defect sites of reducible oxide carriers have been developed [21–23]. Norskov et al. proposed a loading monatomic catalyst into graphene with a single vacancy defect (M@SV). It was found that the slope of the linear relationship between *CO and *CHO binding energy had been changed effectively [24–25]. They also reported that the step of *CO to *CHO was the rate limiting step of all catalysts [26]. Thomas et al. [27] claimed that single-site heterogeneous catalysts has many practical advantages and exhibit very high selectivities, resulting in well-defined molecular products. In addition, the coordination atoms of SACs can change the electronic structure of the active center atoms. After alloying, the adsorption capacity of metal atoms to other substances can be reduced and the product selectivity can be improved. Furtherly it has high dispersion on the carrier and little load. Therefore, the cost is lower than noble metals [28]. Importantly, SACs supported by two-dimensional (2D) N-doped or defective graphene has achieved excellent performance in Reduction Technology of Carbon Dioxide [29–32]. Back et al [33] proposed that CO2RR on transition metals surface was researched extensively, in which Cu was a favorable catalyst for converting CO2 into hydrocarbons and has high Faraday efficiency. Therefore, in this study, we choose SAC-Cu as a highly catalyst to study the reduction of CO2 to CH3OH.

In this work, the mechanisms of CO2 reduction on graphene-supported copper catalysts are examined and compared. Using density functional theory (DFT) combined with a computational hydrogen electrode (CHE) model suggested by Nørskov et al, the free energies of the CO2 reduction intermediates in electrochemical reaction pathways are calculated [34–35]. Moreover, the interesting physical, magnetic and electronic properties of the two catalysts are also examined via the free energy, number of electron transfers per atom, and density of states by established adsorption models of the intermediate species. The differences of observed characteristics have been also discussed. In addition, the “d-band theory” is applied to analyze the activities of the two catalysts. Therefore, this study not only explores two different reduction pathways on graphene-supported copper single-atom catalysts but also deeply understood the design of high-efficiency catalysts from the perspective of expected products selectivity. We hope that the current study can provide a reference for non-noble metal monatomic catalysis of carbon dioxide to methanol by the electrocatalytic method.

2. Computational Modeling

We use the Projected Augmented Wave (PAW) pseudo-potentials to calculate using DFT theory [36] by adopting the Vienna Ab-initio Simulation Package (VASP) [37–39]. The exchange correlation functional is described by Perdew, Burke, and Ernzerhof (PBE) model based on the generalized gradient approximation (GGA) [40]. The adsorption energy on pristine or doped graphene E_{ad} can be calculated as :

$$E_{ad} = E_{molecule} + E_{graphene} - E_{molecule-graphene}$$

1

Where, E*molecule* represents the energy of a single gas molecule, whereas E*graphene* represents the energy of doped graphene, and E*molecule+ graphene* refers to the total energy of the adsorption system. The higher the value of adsorption energy, the stronger the adsorption capacity of intermediate species on the catalyst [41].

The total energies are computed by First-principle DFT calculations to determine the Gibbs free energy (G) of the gas phase species as presented in Eq. (2) [42–44]

$$G = E + ZPE - TS$$

2

Here, E is the total energy of each species calculated by density functional theory. While ZPE and TS are the zero-point energy and vibrational entropy of the corresponding species, respectively. The reasonable vibration mode is determined from the perspective of the first principle, and then the entropy of species is calculated by using the vibration frequency calculated by DFT. The calculation of entropy is approximately, [45–46]

$$S_{\text{vib}} = k_B \sum_{i}^{\#ofmodes} \left(\frac{xi}{e^{x_i} - 1} - ln(1 - e^{-xi})\right)$$

3

wherein, each vibration mode x_i is defined according to the vibration frequency, v_i, as:

$$xi = \frac{\hbar v_i}{k_B T}$$

4

and the ZPE value can also be calculated from v_i as:

$$E_{ZPE} = 1/2 \sum_{i}^{\#of\,\text{models}} \hbar v_i$$

5

Here, k_B is the Boltzmann constant and $\hbar$ is the Planck's constan. And T is standard temperature.

3. Results And Discussion

3.1. Mathematical Models

For graphene supported monoatomic copper catalyst, graphene was used as support, copper as monoatom replaced carbon atom as active center, and the catalyst structure was corrected and optimized by vdW DFT-D2 method [47]. In the calculation process, the kinetic energy cut-off value of the plane-wave is 400 eV and the calculation related to the surface adopts the Monkhorst–Pack mesh, and the grid K-points is 3 ×3 ×1. Furthermore, the convergence threshold is set at -0.05 for the electronic. And for atomic relaxation is 10^{-5} eV. In this model, each graphene layer has a rhombic structure of (7.4 ×7.4 Å), and a vacuum space of 15 Å is set on the Z-axis. A graphene supported monatomic copper catalyst supercell is formed by removing one and two carbon atoms from the graphene structure optimized and reaching the convergence state, and placing one and two copper single atoms in their positions respectively (Fig. 1).

The graphene protocells are selected with a lattice constant of 0.246 nm and expanded into 3*3*1 graphene supercells. There are 18 carbon atoms in the supercell. The thickness of the vacuum layer in the c direction is 15Å to avoid the interlayer interference of graphene. The C-C bond length is 0.142 nm of graphene, and the theoretical thickness of the monolayer atom is 0.34 nm.

3.1.1 Stability of single metal atoms supported on defective graphene

The absolute values of the first ionization energy, electron affinity, and Fermi energy level of graphene and metal copper are presented in Table 1. As known, the electrons are filled to the energy level with lower energy as much as possible. Therefore, in the Cu-G system, the electrons are transferred from the single atom of metal copper to graphene, so that the whole metal copper is positively charged.

Table 1
The first ionization energy (E_1), electron affinity (E_A), Fermi level (E_F), and experimental values of metal work function (Φ) of Graphene and Cu

	E_1	E_A	E_F	Φ
G	4.96	4.34	-4.52	/
Cu	3.89	3.89	-3.86	5.10

The experimental study of catalysis shows that only the strong combination of carrier and metal atoms can prevent the aggregation of metal atoms. Previous studies have found that when metal atoms are adsorbed on defect free graphene, the combination between carrier and metal atoms is weak, which means that metal atoms are easy to diffuse, leading to the formation of metal nanoclusters. Thus, it is very important to introduce defects that can bind closely with the atoms and fix them. Table 2 shows the structural properties and energetic of copper metal atoms supported on defective graphene.

Table 2
Energetic and structural properties of copper metal atoms supported on defective graphene; including the combination energy E_b [Cu], number of charge on copper-atom Q[Cu], the distance of a metal atom above the surface of graphene z[Cu], bond length of Cu−C R[Cu−C], and Cu−C bond strength E[Cu−C].

	Eb[Cu] *(eV)*	*Q[Cu]* *(e)*	*z[Cu]* *(Å)*	*R[Cu-C]* *(Å)*	*E[Cu-C]* *(eV)*
Cu-G3	0.43	0.51	0.94	1.88	*0.39*
Cu-G4	0.46	0.63	0.82	1.91	*0.32*
The combination energy of a copper atom embedded in the graphene is defined as;					

$$E_{\mathrm{b}}[Cu] = E_{G-Vacancy} + \mu_{Cu} - E_{G-\mathrm{Cu}}$$

6

where $E_{G-Vacancy}$ stands for the energy of graphene with a single vacancy, whereas μ_{Cu} represents the chemical potential of Cu in a bulk. While $E_{G-\mathrm{Cu}}$ is the energy of graphene with the substitutional dopant Cu. This energy (E_b[Cu]) represents the adhesion of graphene defect structure to metal atoms. In order to calculate μ_{Cu}, the most stable phase of copper bulk material is selected, where Cu structure is fcc

structure. Thus, the larger the value $E_{\mathrm{b}}[Cu]$, the more stable the doped catalysts is. The distance of one copper atom above the surface of graphene (z[Cu] value) depends on the radius of the bonding atom and the bond strength between the bonding atoms (*E*[Cu–C]). Overall, the results demonstrated in Table show that Cu-G4 is more stable than Cu-G3, however, this may not be beneficial to the catalytic reaction.

3.1.2 Analysis of electronic structure and properties of Cu-G3 and Cu-G4

In monatomic catalytic reactions, the strong interaction between active metals and substrate will greatly affect the electronic structure of these metal atoms. The intrinsic graphene is a semi-metallic crystal with Dirac point K of Fermi energy level. However, for a 3 ×3 graphene supercell structure, the Dirac point is transferred from vertex K of graphene's reduced Brillouin region to Gamma (G) point region. Moreover, the bandgap at the Fermi level is still close to 0 eV, which is consistent with the zero value of the density of states at the Fermi level. This means that the energy band of intrinsic graphene is approximately linear, at which the conduction and valence bands intersect, as well as the bottom of the conduction band and the top of the valence band intersect at the Fermi level, showing the semi-metallic characteristic of zero bandgaps. The semiconductor with a zero bandgap cannot be used directly. Doping can open the energy band and introduce the bandgap, which is conducive to the catalytic reaction.

Figure 2 shows the band structures and density of states (DOS) of the Cu-G3 and Cu-G4 catalysts. The results showed that the single copper atom is oxidized by three carbon atoms and four carbon atoms, respectively. The neutral copper atoms have corresponding electronic states near the Fermi level, however, a redox reaction occurs when interacting with carbon atoms, resulting in the gain and loss of electrons. It can be also seen that the d-electrons of copper are converted to carbon, and the p orbital of the C atom acquires the electrons of the copper atom. Compared with a single copper catalyst, the Cu 3d states reach their peak at the Fermi level at which the density of states prominently exists. Compared with DOS of Fig. 2(a,b), it can be seen that the bonding of the latter is significantly more than that of the former below the Fermi level, and the density of states of the former is significantly more than that of the latter at the Fermi level. Furtherly, the contribution of Cu of the former is large (the blue line). This can also be seen from the energy band diagram on the left. The peak of the former is obviously opened and the shadow is more obvious. There is an obvious gap between the conduction band and valence band at the high symmetry point G, which is conducive to the catalytic reaction.

Figure 3 displays the atomic charge coloring diagram of the Cu-G3 and Cu-G4 catalysts. As can be seen from Fig. 3, after doping copper atoms, copper atoms lose 0.51e and 0.63e charges, and copper atoms are positively charged together with the charges of adjacent carbon atoms. The charge lost by the surface atom is mainly transferred to the nearest carbon atom, which is consistent with the fact that the electronegativity of the Cu atom is less than that of the C atom. Comparing the atomic charge coloring diagrams of Cu-G3 and Cu-G4 as shown in Fig. 3, the carbon atoms of No. 9, 14, and 16 are most affected by the doped copper atoms and obtained the most electrons among all carbon atoms. The darker the blue, the more electrons the C atom obtained. It is also clear that the degree of co-ownership of

C and Cu atoms in the Cu-G4 catalyst is higher than that of the Cu-G3 catalyst. The specific atomic charge values are listed in Table S2-3 and Figure S1-2 in Appendix A.

Figure 4 depicts the differential charge density diagram of doped graphene of the Cu-G3 and Cu-G4 catalysts. In Fig. 4., the yellow bonds indicate an increase in the charge density, whereas the blue bonds adversely show a decrease in the charge density. Besides, a new chemical bond is formed between C and Cu atoms, Cu loses electrons, and C obtains electrons. It can be also seen from the charge density distribution diagram that the charge density distribution around Cu atoms is greatly changed. Also, the electron cloud is gathered around the impurity atoms, and the bonding ability between atoms is gradually enhanced. Moreover, it is revealed also that the overlap of electron cloud between Cu-G4 atoms is much clearer than that between Cu-G3 atoms. On the other hand, the results show that doping can be improved the conductivity of graphene. For Cu-G4, the graphene after removing two carbon atoms is doped with copper atoms with a larger radius, which makes the interaction between copper and carbon atoms highly stronger with stable ionic bonds. Besides, more overlap between C and Cu is observed that is conducive to the electron transfer, which is consistent with the previous energy band analysis results as discussed in Fig. 4.

Figure 5 presents the density of states diagram of the intrinsic and doped graphene. Comparing the density of states diagram of the doped system with that of the intrinsic graphene system as seen in Fig. 5. It can be seen that the total density of states after doping is much larger than that of the intrinsic graphene, indicating that the number of energy levels and electronic states of the doped system is increased. At the same time, the atomic orbital of Cu is reduced the conduction bandwidth at the bottom of the conduction band. Moreover, the results also revealed the doping effect is significantly increased the sharing degree between electrons and enhanced the local properties of materials as well as improved the catalytic performance. For Cu-G3, it is mainly the interaction between the p orbital of C and the s-d-p orbital of Cu. The main bonding between C with Cu is about − 4 eV, and the bonding is Cu (s-d) with C(p) along the Z direction, that is σ bond. Compared with Cu-G3, the main difference is the p and d orbitals of Cu, which have a deeper impact on the anti-bond orbitals of Cu-G4. Hence, this will weaken the binding between the catalyst and the intermediate product, resulting in a slightly higher energy barrier for subsequent hydrogenation for the Cu-G4 than Cu-G3. The latter results are consistent with the results of energy band and density of states analyses in Figs. 2 and 4.

3.2. CO2 to CH3OH performance

3.2.1 Electrochemical reduction reaction of CO2 on Cu-G3

Two initial intermediates were produced in the initial electrochemical reduction reaction of carbon dioxide hydrogenation; namely *COOH and *HCOO are labeled by formate path and carboxylate path (*COOH-pathways and *HCOO-pathways) due to different reductive pathways of the two intermediates. Herein, the different reduction pathways on graphene-supported copper single-atom (Cu/G3) catalysts will be analyzed in detail.

The electrocatalytic reduction of CO2 on triple coordinated Cu-G3 catalyst was studied for the first time to determine the CO2 reduction mechanism of Cu single atom supported on single vacancy defective graphene. The relative free energy of each step of HCOO pathway on Cu-G3 catalyst is shown in Fig. 6 (a). And the values of free energy calculations are clearly shown in Table S1(a-b) in Appendix A. The HCOO reduction path on Cu-G3 catalyst can be clearly observed from Fig. 6 (a) as follows: CO2 → *HCOO → *HCOOH → *CHO → *CH2O → *CH3O → CH3OH(g). The relative free energy of each step of COOH pathway of CO2 reduction on the Cu-G3 catalyst surface was given on Fig. 6(b) The determined COOH reduction path is observed as follows: CO2 → *COOH → *CO → results trend *CHO → *CH2O → *CH3O → CH3OH(g). Furthermore, the hydrogenation of *CO to *CHO is a potential limiting step in thermodynamics in the electrochemical reduction reaction. It is worthing to mention that the trend of results on Fig. 6 (a) show no difference with that by Lee et al [48] research work finding, which shows the accuracy of the present results. Figure 7 shows the species structure of the most likely intermediates on Cu-G3 catalyst. These intermediates are connected in series to form the most likely reaction pathways for two different reactions. The results in Fig. 7 also indicated that the HCOO is clearly linked by O while the COOH is bonded by C within a single metallic binding site. This also leads to the difference of intermediate species and the two paths that produce different reaction free energy.

In summary, based on the obtained results of mechanism analysis of reaction path on the Cu-G3 catalyst, two endothermic reactions have been observed along the carboylate path where the highest energy barrier (1.1 eV) corresponds to a conversion step of *CO to *CHO. In contrast, the formate path fulfilled a more stable configuration, with a free energy barrier of 0.41 eV, indicating an endergonic step, which considerably reduced to methanol rather than being easily released as HCOOH on Cu/G3 catalyst.

3.2.2 Electrochemical reduction reaction of CO2 on Cu-G4

On the other hand, the hydrogenation of CO2 to methanol on Cu-G4 catalyst was also studied to determine the detailed mechanism of CO2 reduction reaction on graphene supported single copper atom. The relative free energy of each step of HCOO pathway on Cu-G4 catalyst is shown in Fig. 8 (a). And the values of free energy calculations are tabulated in Table S1(c-d) in the supplementary document. The detailed electrochemical reduction pathway are as follows: CO2 → *HCOO → *HCOOH → *CHO → *CH2O → *CH3O → CH3OH (g). The first step of hydrogenation of carbon dioxide, from CO2 to *HCOO, is the potential limiting step (0.5 eV) of the whole reaction path. While the relative free energy of COOH pathway of CO2 reduction on the Cu-G4 catalyst surface was given on Fig. 8(b).

The specific reaction path along *COOH on Cu-G4 catalyst is as follows, CO2 → *COOH →* CO → *CHO → *CH2O → *CH3O → CH3OH (g), given that *CO → *CHO of potential-limiting step (1.13 eV). These results are in good agreement with the analytical results reported by Back et al [33], which emphasized the correctness of the present simulations. Similar to the comparison of HCOO and COOH path mechanisms on Cu-G3 catalyst previously discussed in Fig. 7. Figure 9 shows the comparison of the most appropriate mechanisms for the HCOO and COOH on the Cu/G4 catalyst.

3.3 DOS profiles

3.3.1 Initial protonation steps: selectivity for CO2RR vs HER on the Cu-G3/4

The electro-reduction of CO2 begins with the hydroprotonation of adsorbed CO2 and forms carboxyl or formate on graphene based copper catalyst respectively (see Fig. 6 and Fig. 8). However, three reactions may occur on graphene based catalysts. The first two are hydrogenation protonation to form carbon-oxygen-hydrogen species, COOH or HCOO and the third is that hydrogen (H2) is reduced to hydrogen protons (H+). Wherefore, in order to know the degree to which the three substances are easy to produce, we need to compare the free energy changes of the three reactions, as presented in Fig. 10. From Fig. 10, the results unveiled that the formation trend of the first two species is more favorable than that of hydrogen protons. Moreover, the catalyst with a single metal vacancy can effectively occur along the carbon dioxide hydrogenation reduction reaction rather than hydrogen evolution reaction.

Then, the reaction continues to be further hydrogenated, and the reaction free energy of the product obtained by the second step hydrogenation is calculated and compared. For Cu-G3, as seen in Fig. 10, the carboxylate path (*COOH-pathway) reveal that *CO is produced by the protonation of *COOH. However, there are two reactions in the next step, either the adsorbed CO is desorbed from the catalyst, or the hydrogenation is continued to produce another substance, *HCOOH. This mainly depends on the variation values of the two free energies. On this catalyst, the latter is preferred. For formate path (*HCOO-pathway), there is only one way to continue hydrogenation, that is, to continue to generate HCOOH generally.

Similarly, for Cu-G4, whether it is the carboxylate or formate path, the reaction intermediates of continuous hydrogenation are the same. The difference between them is that the difficulty of the reaction is different, which is also determined by the thermodynamic Gibbs free energy of the reaction.

3.3.2 Fundamental analysis of the products (CO or CHO) generation

From the results previously presented in Fig. 6 and Fig. 8, the limiting steps of the two investigated catalysts are obtained to be CO* → CHO* of the *COOH-pathway. Therefore, it is necessary to determine the stability of the intermediate products *CO and *CHO on the surface of graphene supported monatomic copper (Cu-G3/4) and bulk copper Cu(111). Perhaps the physical forms of their adsorption on these two kinds of catalysts can explain that monatomic copper is better than bulk copper. The optimized geometries of the *CO and *CHO species that adsorbed in the catalyst surfaces of Cu (111), Cu-G3, and Cu-G4 are shown in Fig. 11.

It can be clearly seen from Fig. 11 that for the bulk copper 111 surface catalyst, both surface copper atoms are bonded to the carbon of *CO. However, during further hydrogenation, only one Cu atom is

bonded to the carbon atom in *CHO, resulting in the loss of stability of relative free energy from *CO to *CHO. For Cu-G3/4, it is observed that only one Cu atom binds to the carbon atoms of *CO and *CHO, which is also the reason why the former is more active than the latter. Moreover, it also found that the longer the bond length, the smaller the free energy required to produce CHO. And the bond length of Cu-C on Cu-G3 is longer than *CO-Cu-G4 and *CHO-Cu-G3/4, respectively. Furthermore, it also observed that the single-atom catalyst is broken the linear constraint of the traditional bulk metal on the adsorption/desorption relationship of intermediate products in the CO2 reduction reaction. The specific changes of Gibbs free energy from *CO to *CHO on Cu (111), Cu-G3, and Cu-G4 catalysts are shown in Fig. 12. It is shown that the longer the bond length, the easier the subsequent reaction and the lower the potential barrier. It is obtained that the free energies of *CO to *CHO for the Cu-G3, and Cu-G4 catalysts are estimated to be1.1eV and 1.13eV, respectively. Also, the bond lengths of the Cu-G3 and Cu-G4 catalysts are found to be 1.68 A and 1.52A, respectively. The latter results are conformable with the previous energy analysis results reported in the literature.

3.3.3 Fundamental analysis using “d-band theory” and PDOS

The d-band center can be used as a "descriptor" to describe the adsorption of the interaction between the catalyst and model molecule. According to the d-band theory, the change of atomic bandwidth will move the center of d-band, and then affect the coupling between molecular orbital to the d-states.[49]. And therefore, the doping of transition metals (narrow d-band) can be enhanced the charge non-uniform distribution of the material, improve the density of states at the Fermi level, and thus improve the d-band central energy level of Cu-G to make it close to the Fermi level. As a result, it leads to a drastic shift of the d-band center, which makes a significant change in the adsorption energy and enhances the adsorption capacity of the catalyst surface and intermediates, as well as regulates the CO2RR activity of the catalyst [50]. Figure 13 represents a comparison of the d-band centers of Cu atoms before and after CO adsorption. It is observed that the closer the d-band center is to the Fermi level, the stronger the activity is. In contrast, the farthest the d-band center is from the Fermi level, the weaker the activity is. As can be seen from Fig. 13, the d-band center of Cu(111)-CO is closer to the Fermi level than that of graphene supported monatomic catalyst. This is mainly because the anti bond orbital of monatomic catalyst is filled more, resulting in the average adsorption capacity for intermediate products compared with bulk copper. However, it observed that there is a linear constraint relationship between the adsorption and desorption of the intermediates in the catalytic reaction of the bulk metal catalysts. Additionally, compared with Cu-G3-CO, the d-band center of the Cu-G4-CO is closer to the Fermi level, indicating that the adsorption of the former is stronger, and the energy barrier for the next reaction is higher compared to that of Cu-G3-CO.

Figure 14 depicts the variations of projected density of states (PDOS) of the Cu-G3 and Cu-G4 catalysts upon *CO adsorption. It is obtained that the peaks above the Fermi level are identified numerically which are symbolized to be 1.0, 2.0, and 3.0, respectively. From the optimized structure, it can be in Fig. 15 seen that the specific overlapping density diagram of C and Cu orbits is highlighted and the interaction between Cu and C atoms is the vertical orbit. On the whole, it is revealed that the d electron of Cu is

mainly bonded particularly over the three coordinated copper monatomic Cu-G3 catalyst at the peak of NO. 2 above the Fermi level as shown in Fig. 14. Compared with the results of the relative free energy diagram that previously presented in Fig. 6(a), it can be indicated that the major bonding interaction between the *CO and Cu-G3/4 is the Cu(d_z^2)- Cu(p_z)- C(p_z) σ bond along the z-direction which is obtained to be -7 eV at the peak (NO. 2) above the Fermi level. While the second peak corresponded to the bonding interaction between Cu(spd) and C(p) is about − 4 eV. Furthermore, it is also indicated that there is an interaction between the Cu and C atoms is observed above the Fermi level because the PDOS of O does not change upon the*CO adsorption. On the other hand, for the Cu-G4, there is obvious that an antibonding on the Cu-s-p and C-s upon the*CO adsorption is found to be 10eV, which weakens the binding between the catalyst and the intermediate product, resulting in a slightly higher energy barrier for the subsequent hydrogenation of the Cu-G4 than that of Cu-G3. However, at the – 4 eV level, the p and d orbitals of Cu have a deeper impact on the anti-bond orbitals. The latter result clearly explains the difference in the free energy from *CO to *CHO on the two proposed catalysts.

Figure 15 displays the PDOS of the Cu-G3 and Cu-G4 catalysts upon *CHO adsorption. It is observed that for Cu-G3/4-CHO, the orbital contribution for *CHO binding is also the σ bonding interactions along the z-direction similar to Cu-G3/4-*CO. It can be also seen that more electrons are transferred to C within the Cu-G4/CHO and the Cu-G4 is weaker than Cu-G3 on the interaction of CHO, in particular near the Fermi level. More specifically, it can be clearly observed that the d orbital of Cu for the Cu-G3 has a clear and sharp peak (NO.2), as a result of the interaction with O. Further, the p orbital of O obviously overlaps with the total density of states (Peak NO.1 and Peak NO.2), which interprets the intermediate *OCH2 with the catalyst are bonded between O and Cu. However, for Cu-G4, it can be revealed that the interaction between the p orbital (NO.1–3) of C and the p-d orbital (NO.1–3) of Cu is more profound, while the effect of O for the Cu-G4 is weaker compared to that of Cu-G3. This is mainly due to that the copper atoms transferred more electrons to carbon atoms on the smooth Cu-G4 catalyst when CHO is adsorbed. In addition, it can be seen from Fig. 15 (b) that the s orbital of the Cu atom in the Cu-G3 is significantly involved in bonding than that in the Cu-G4, especially at the Fermi level. And more importantly, the s-p electrons of copper filled the anti-bond orbital, which occupied the anti-bond orbital, weakened the binding with CHO, and led to the spontaneous occurrence of the subsequent reduction reaction.

4. Conclusions

In this paper, the electrocatalytic performance reduction of CO_2 to methanol on two types of graphene-supported single-atom-copper catalysts namely; Cu/G3 and Cu/G4 using the first-principles model integrated with the computational hydrogen electrode approach. The main findings of this work are deduced as follows.

1. From the electrochemical reduction results of CO2, the three coordinated monatomic copper (Cu-G3) is slightly oxidized, whereas the four coordinated monatomic copper (Cu-G4) is heavily oxidized. Consequently, the Cu-G3 catalyst is strongly preferred as an effective electrocatalytic for the conversion of CO2 to CH3OH.

2. From the band structures and density of states (DOS) analyses of the Cu-G3/4, it revealed that the number of electronic states is increased and the DOS of graphene is redistributed by Cu doping. A strong charge density region is formed near the doped Cu atom, and electron clouds are collected around the impurity Cu atoms. The Cu atom lose 0.51e and 0.63e charges, while the adjacent carbon atoms obtained charges on Cu-G3/4.
3. Two various pathways (*HCOO and *COOH) on the two proposed catalysts (Cu-G3 and Cu-G4) are explored based on the initially produced intermediates. The Cu-G3/G4 catalysts robustly promote the HCOO* pathway with an energy barrier of 0.41 eV (*HCOOH → *CHO) and 0.50 eV (*CO_2 → *HCOO). However, the rate-limiting step for the *COOH pathway on Cu-G3/G4 catalysts is (*CO → *CHO), with limiting potentials of 1.1 eV and 1.13 eV, respectively.
4. The bond lengths of Cu-C are estimated to be 1.68 Å and 1.52 Å for Cu-G3/G4 catalysts, respectively. Also, the free energies of *CO to *CHO are lower than that of Cu (111) which are found to be 1.1eV and 1.13eV, respectively. The d-band centers of Cu atoms before and after CO adsorption are compared. It is observed that the closer the d-band center is to the Fermi level, the stronger the activity is. In contrast, the farthest the d-band center is from the Fermi level, the weaker the activity is.
5. The major bonding interaction between *CO and Cu-G3/G4 is the Cu(d_z^2)- Cu(p_z)- C(p_z) σ bond along the z-direction with an energy barrier of -7 eV. For Cu-G4, the antibonding between Cu-s-p and C-s upon CO adsorption is about 10 eV, which weakens the binding between the catalyst and the intermediate product, resulting in a slightly higher energy barrier for subsequent hydrogenation than Cu-G3. Moreover, the s-p electrons of copper have filled the anti-bond orbital and weakened the binding with *CHO, leading to a spontaneous occurrence of the subsequent reduction reaction.

Declarations

Declaration of Competing Interest

The authors declare that they have no known competing financial interests or personal relationships that could have appeared to influence the work reported in this paper.

Acknowledgments

This work is supported by Key Research and Development Project in Tianjin (20YFYSGX00020). Science and Technology Service Network Initiative of Chinese Academy of Sciences (KFJ-STS-QYZD-2021-02-006).

Appendix A. Supplementary material

Supplementary data to this article can be found online at…

References

1. Yu H, Li J, Zhang Y, et al. Three-in-one oxygen vacancies: whole visible-spectrum absorption, efficient charge separation, and surface site activation for robust CO_2 photoreduction[J]. Angewandte Chemie International Edition, 2019, 58(12): 3880–3884.
2. Cui H, Guo Y, Guo L, et al. Heteroatom-doped carbon materials and their composites as electrocatalysts for CO_2 reduction[J]. Journal of Materials Chemistry A, 2018, 6(39): 18782–18793.
3. Tu W, Zhou Y, Zou Z. Photocatalytic conversion of CO_2 into renewable hydrocarbon fuels: state-of-the-art accomplishment, challenges, and prospects[J]. Advanced Materials, 2014, 26(27): 4607–4626.
4. Zhang X, Zhang Z, Li J, et al. Ti_2 CO_2 MXene: a highly active and selective photocatalyst for CO_2 reduction[J]. Journal of Materials Chemistry A, 2017, 5(25): 12899–12903.
5. Aresta M, Dibenedetto A, Angelini A. Catalysis for the valorization of exhaust carbon: from CO_2 to chemicals, materials, and fuels. Technological use of CO_2[J]. Chemical reviews, 2014, 114(3): 1709–1742.
6. Zhao G, Wang H, Liu G. Recent advances in chemically modified electrodes, microfabricated devices and injection systems for the electrochemical detection of heavy metals: A review[J]. Int. J. Electrochem. Sci, 2017, 12(9): 8622–8641.
7. Kuhl K P, Hatsukade T, Cave E R, et al. Electrocatalytic conversion of carbon dioxide to methane and methanol on transition metal surfaces[J]. Journal of the American Chemical Society, 2014, 136(40): 14107–14113.
8. Kuhl K P, Cave E R, Abram D N, et al. New insights into the electrochemical reduction of carbon dioxide on metallic copper surfaces[J]. Energy & Environmental Science, 2012, 5(5): 7050–7059.
9. Hao J, Shi W. Transition metal (Mo, Fe, Co, and Ni)-based catalysts for electrochemical CO_2 reduction[J]. Chinese Journal of Catalysis, 2018, 39(7): 1157–1166.
10. Medford A J, Vojvodic A, Hummelshøj J S, et al. From the Sabatier principle to a predictive theory of transition-metal heterogeneous catalysis[J]. Journal of Catalysis, 2015, 328: 36–42.
11. Back S, Lim J, Kim N Y, et al. Single-atom catalysts for CO_2 electro-reduction with significant activity and selectivity improvements[J]. Chemical science, 2017, 8(2): 1090–1096.
12. Wang Y, Mao J, Meng X, et al. Catalysis with two-dimensional materials confining single atoms: concept, design, and applications[J]. Chemical reviews, 2018, 119(3): 1806–1854.
13. Novoselov K S, Geim A K, Morozov S V, et al. Electric field effect in atomically thin carbon films[J]. science, 2004, 306(5696): 666–669.
14. Zhang Y, Tan Y W, Stormer H L, et al. Experimental observation of the quantum Hall effect and Berry's phase in graphene[J]. nature, 2005, 438(7065): 201–204.
15. Li X, Cai W, An J, et al. Large-area synthesis of high-quality and uniform graphene films on copper foils[J]. science, 2009, 324(5932): 1312–1314.
16. Lim D H, Negreira A S, Wilcox J. DFT studies on the interaction of defective graphene-supported Fe and Al nanoparticles[J]. The Journal of Physical Chemistry C, 2011, 115(18): 8961–8970.

17. Lim D H, Wilcox J. Mechanisms of the oxygen reduction reaction on defective graphene-supported Pt nanoparticles from first-principles[J]. The Journal of Physical Chemistry C, 2012, 116(5): 3653–3660.
18. Liu J. Catalysis by supported single metal atoms[J]. Acs Catalysis, 2017, 7(1): 34–59.
19. Yang X F, Wang A, Qiao B, et al. Single-atom catalysts: a new frontier in heterogeneous catalysis[J]. Accounts of chemical research, 2013, 46(8): 1740–1748.
20. Qiao B, Wang A, Yang X, et al. Single-atom catalysis of CO oxidation using Pt1/FeOx[J]. Nature chemistry, 2011, 3(8): 634–641.
21. Wang A, Li J, Zhang T. Heterogeneous single-atom catalysis[J]. Nature Reviews Chemistry, 2018, 2(6): 65–81.
22. Nie L, Mei D, Xiong H, et al. Activation of surface lattice oxygen in single-atom Pt/CeO2 for low-temperature CO oxidation[J]. Science, 2017, 358(6369): 1419–1423.
23. Liu G, Robertson A W, Li M M J, et al. MoS2 monolayer catalyst doped with isolated Co atoms for the hydrodeoxygenation reaction[J]. Nature chemistry, 2017, 9(8): 810–816.
24. Evans M G, Polanyi M. Inertia and driving force of chemical reactions[J]. Transactions of the Faraday Society, 1938, 34: 11–24.
25. Cheng J, Hu P, Ellis P, et al. Brønsted – Evans – Polanyi relation of multistep reactions and volcano curve in heterogeneous catalysis[J]. The Journal of Physical Chemistry C, 2008, 112(5): 1308–1311.
26. Kirk C, Chen L D, Siahrostami S, et al. Theoretical investigations of the electrochemical reduction of CO on single metal atoms embedded in graphene[J]. ACS central science, 2017, 3(12): 1286–1293.
27. Thomas J M, Raja R, Lewis D W. Single-site heterogeneous catalysts[J]. Angewandte Chemie International Edition, 2005, 44(40): 6456–6482.
28. Su X, Yang X F, Huang Y, et al. Single-atom catalysis toward efficient CO2 conversion to CO and formate products[J]. Accounts of chemical research, 2018, 52(3): 656–664.
29. Wang Y, Mao J, Meng X, et al. Catalysis with two-dimensional materials confining single atoms: concept, design, and applications[J]. Chemical reviews, 2018, 119(3): 1806–1854.
30. Wang T, Zhao Q, Fu Y, et al. Carbon-rich nonprecious metal single-atom electrocatalysts for CO2 reduction and hydrogen evolution[J]. Small Methods, 2019, 3(10): 1900210.
31. Guo J, Huo J, Liu Y, et al. Nitrogen-doped porous carbon-supported nonprecious metal single-atom electrocatalysts: from synthesis to application[J]. Small Methods, 2019, 3(9): 1900159.
32. Wu J, Sharifi T, Gao Y, et al. Emerging Carbon-Based Heterogeneous Catalysts for Electrochemical Reduction of Carbon Dioxide into Value-Added Chemicals[J]. Advanced Materials, 2019, 31(13): 1804257.
33. Back S, Lim J, Kim N Y, et al. Single-atom catalysts for CO_2 electroreduction with significant activity and selectivity improvements[J]. Chemical science, 2017, 8(2): 1090–1096.
34. Peterson A A, Abild-Pedersen F, Studt F, et al. How copper catalyzes the electroreduction of carbon dioxide into hydrocarbon fuels[J]. Energy & Environmental Science, 2010, 3(9): 1311–1315.

35. Nørskov J K, Rossmeisl J, Logadottir A, et al. Origin of the overpotential for oxygen reduction at a fuel-cell cathode[J]. The Journal of Physical Chemistry B, 2004, 108(46): 17886–17892.
36. Kresse G, Joubert D. From ultrasoft pseudopotentials to the projector augmented-wave method[J]. Physical review b, 1999, 59(3): 1758.
37. Kresse G, Hafner J. Ab initio molecular dynamics for liquid metals[J]. Physical review B, 1993, 47(1): 558.
38. Kresse G, Hafner J. Ab initio molecular-dynamics simulation of the liquid-metal–amorphous-semiconductor transition in germanium[J]. Physical Review B, 1994, 49(20): 14251.
39. Kresse G, Furthmüller J. Efficiency of ab-initio total energy calculations for metals and semiconductors using a plane-wave basis set[J]. Computational materials science, 1996, 6(1): 15–50.
40. J.P. Perdew, K. Burke, M. Ernzerhof, Generalized gradient approximation made simple, Phys. Rev. Lett. 77 (1996) 3865.
41. Ghosh A, Subrahmanyam K S, Krishna K S, et al. Uptake of H2 and CO2 by graphene[J]. The Journal of Physical Chemistry C, 2008, 112(40): 15704–15707.
42. Michalsky R, Zhang Y J, Peterson A A. Trends in the hydrogen evolution activity of metal carbide catalysts[J]. ACS Catalysis, 2014, 4(5): 1274–1278.
43. Denny S R, Tackett B M, Tian D, et al. Exploring electrocatalytic stability and activity of unmodified and platinum-modified tungsten and niobium nitrides[J]. International Journal of Hydrogen Energy, 2020, 45(43): 22883–22892.
44. Ma Y, He Z, Wu Z, et al. Galvanic-replacement mediated synthesis of copper-nickel nitrides as electrocatalyst for hydrogen evolution reaction[J]. Journal of Materials Chemistry A, 2017, 5(47): 24850–24858.
45. Wang S, Li B, Li L, et al. Highly efficient N2 fixation catalysts: transition-metal carbides M 2 C (MXenes)[J]. Nanoscale, 2020, 12(2): 538–547.
46. Gokhale A A, Kandoi S, Greeley J P, et al. Molecular-level descriptions of surface chemistry in kinetic models using density functional theory[J]. Chemical Engineering Science, 2004, 59(22–23): 4679–4691.
47. Grimme S. Semiempirical GGA-type density functional constructed with a long-range dispersion correction[J]. Journal of computational chemistry, 2006, 27(15): 1787–1799.
48. Lee C M, Senthamaraikannan T G, Shin D Y, et al. Graphite-supported single copper catalyst for electrochemical CO_2 reduction: A first-principles approach[J]. Computational and Theoretical Chemistry, 2021, 1201: 113277.
49. Ruban A, Hammer B, Stoltze P, et al. Surface electronic structure and reactivity of transition and noble metals[J]. Journal of Molecular Catalysis A: Chemical, 1997, 115(3): 421–429.
50. Zhao Z, Lu G. Cu-based single-atom catalysts boost electro-reduction of CO_2 to CH_3OH: First-principles predictions[J]. The Journal of Physical Chemistry C, 2019, 123(7): 4380–4387.

Figures

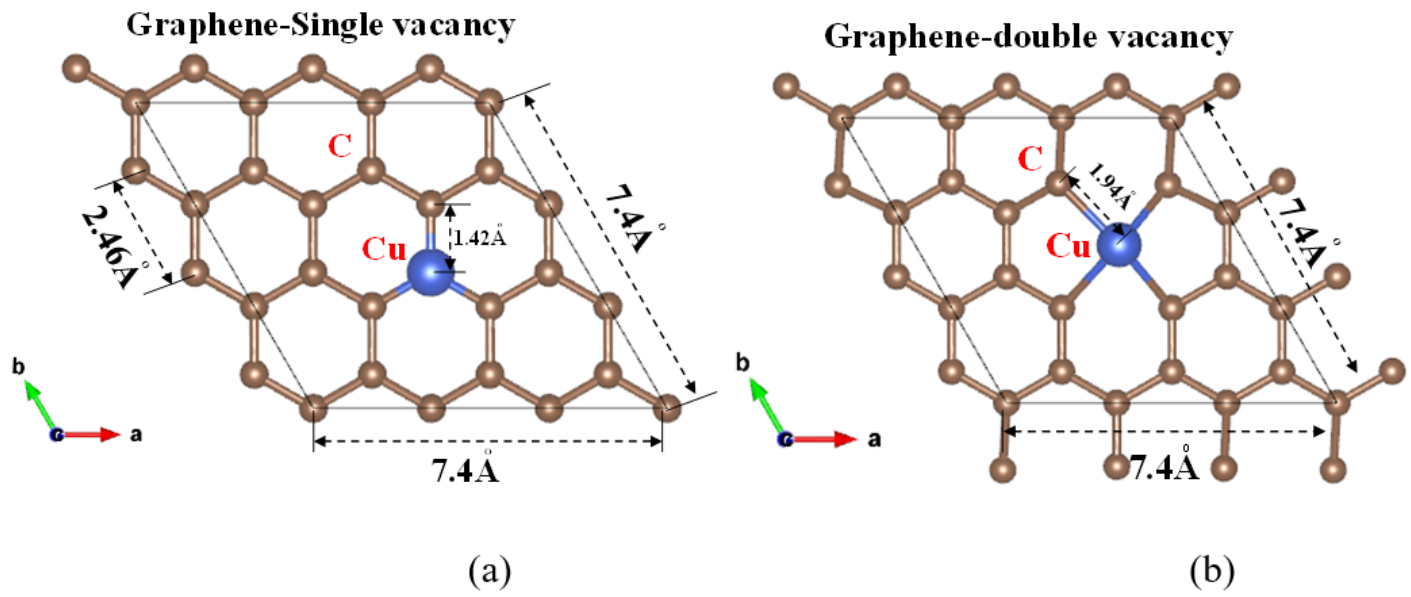

Figure 1

(a) Views of the Cu-G3 catalyst. (b) Views of the Cu-G4 catalyst

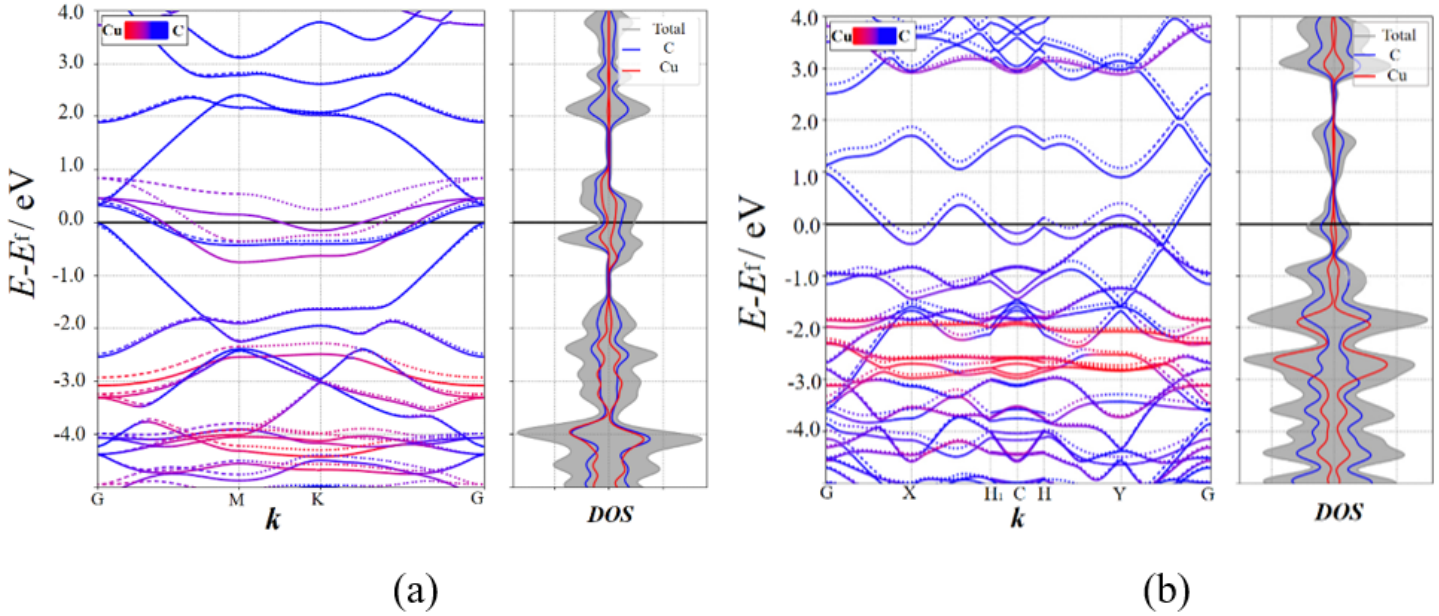

Figure 2

Band structures and the DOS of the doped graphene: (a) Cu-G3; (b) Cu-G4.

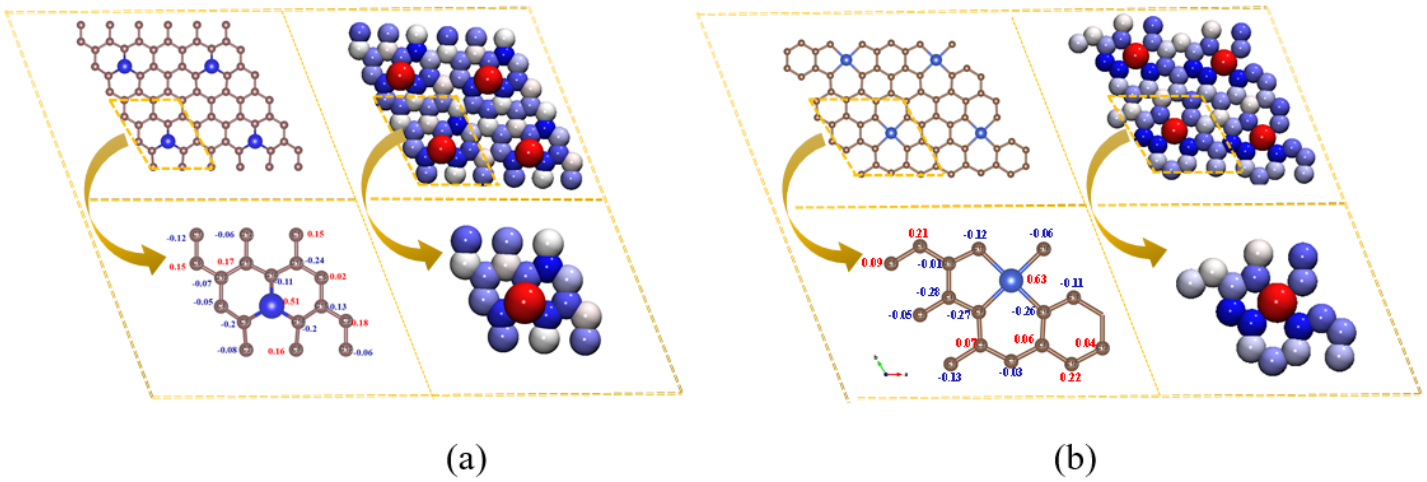

Figure 3

Atomic charge coloring diagram (a) Cu-G3 (b) Cu-G4. (The blue bonds are negatively charged and the red bonds are positively charged).

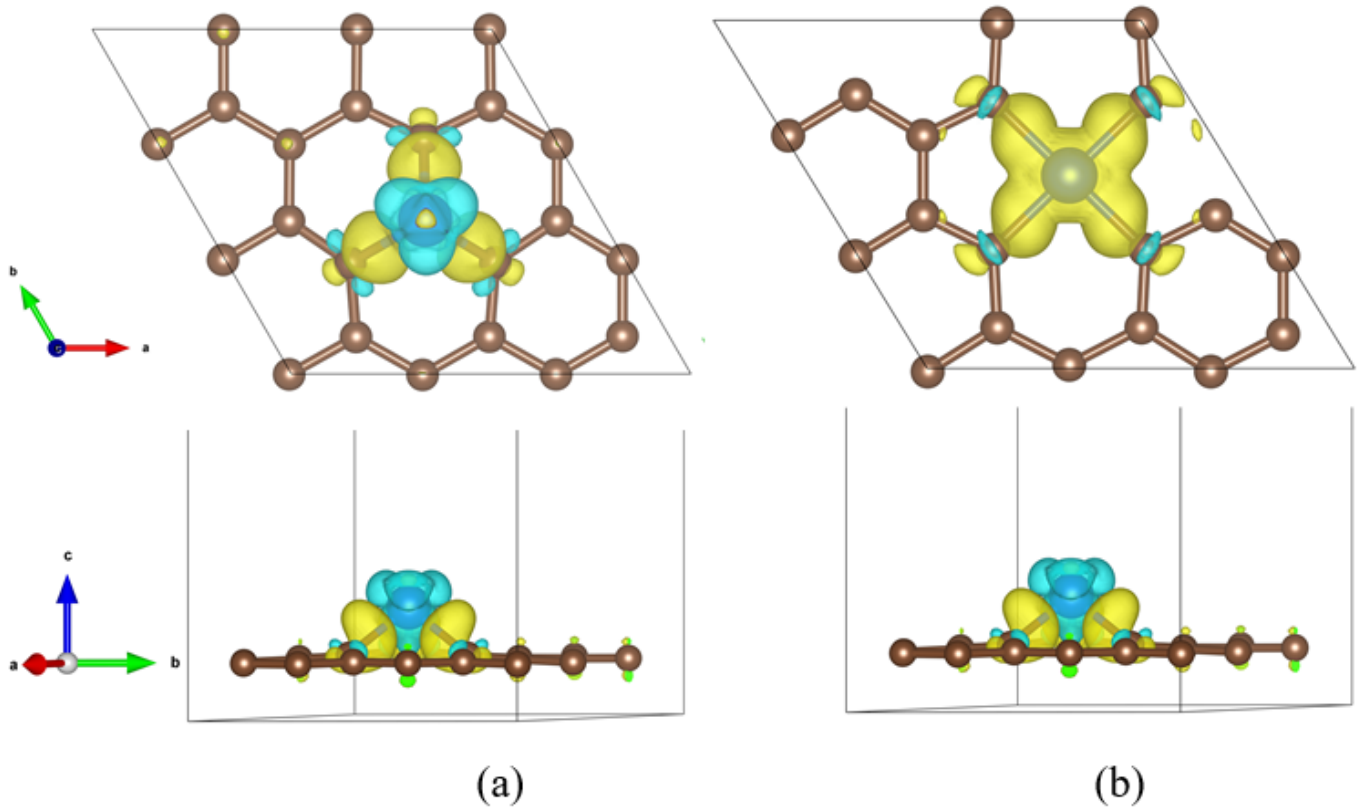

Figure 4

The differential charge density diagram (a) Cu-G3 (b) Cu-G4. The yellow bonds indicate an increase in the charge density and the blue bonds refer to a decrease in charge density, isosurface value=0.04e/bhor^3

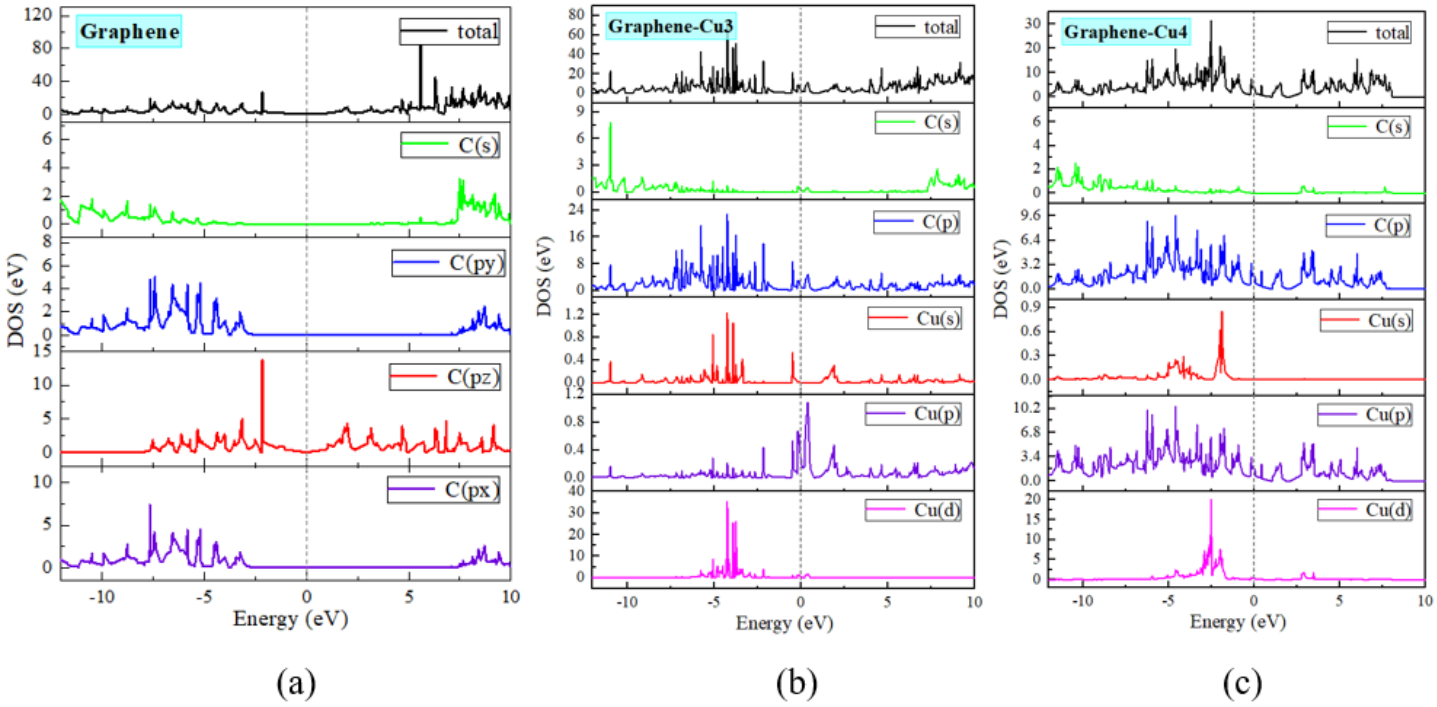

Figure 5

Density of states diagram of the intrinsic and doped graphene (a) G (b) Cu-G3 (c) Cu-G4

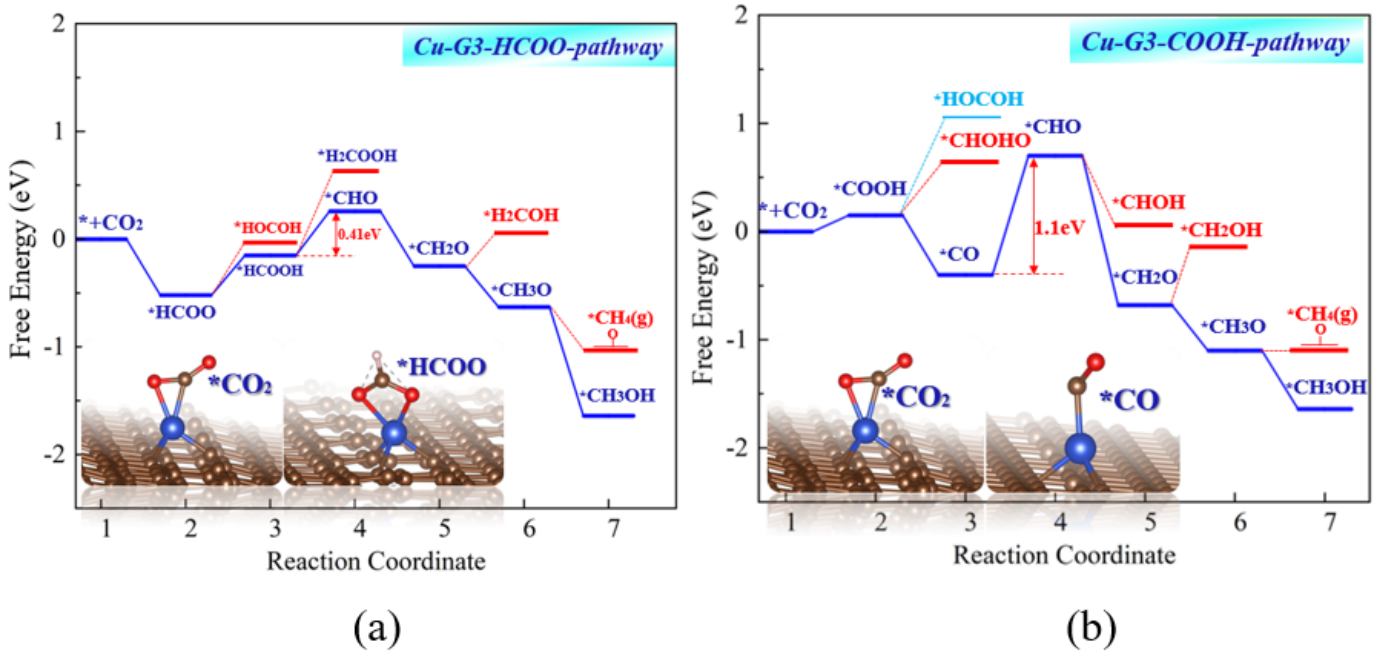

Figure 6

The free energy for CO2RR (a) Cu-G3-HCOO-pathway and (b) Cu-G3-COOH-pathway

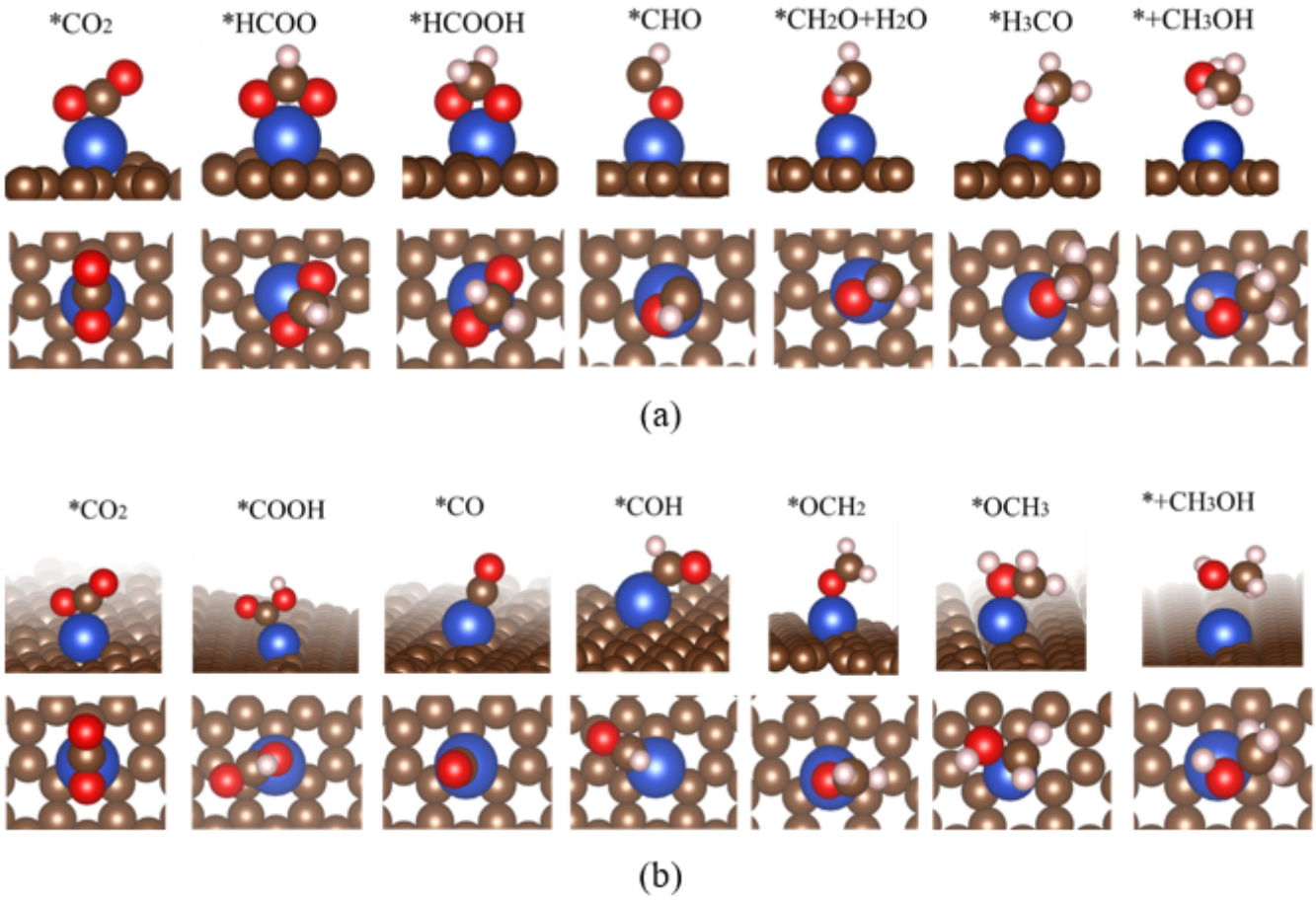

Figure 7

Adsorption structure of intermediate products in two reaction paths for (a) Cu-G3-HCOO-pathway and (b) Cu-G3-COOH-pathway

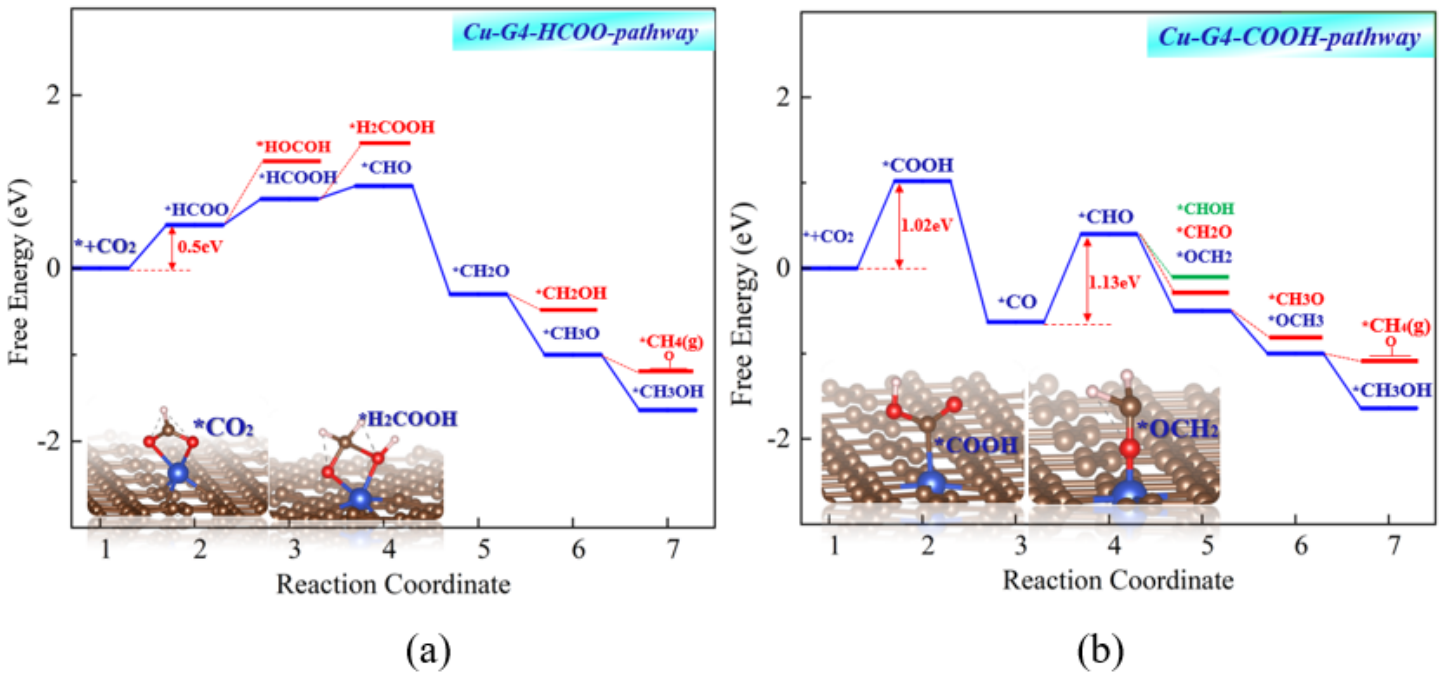

Figure 8

The free energy for CO2RR (a) Cu-G4-HCOO-pathway and (b) Cu-G4-COOH-pathway

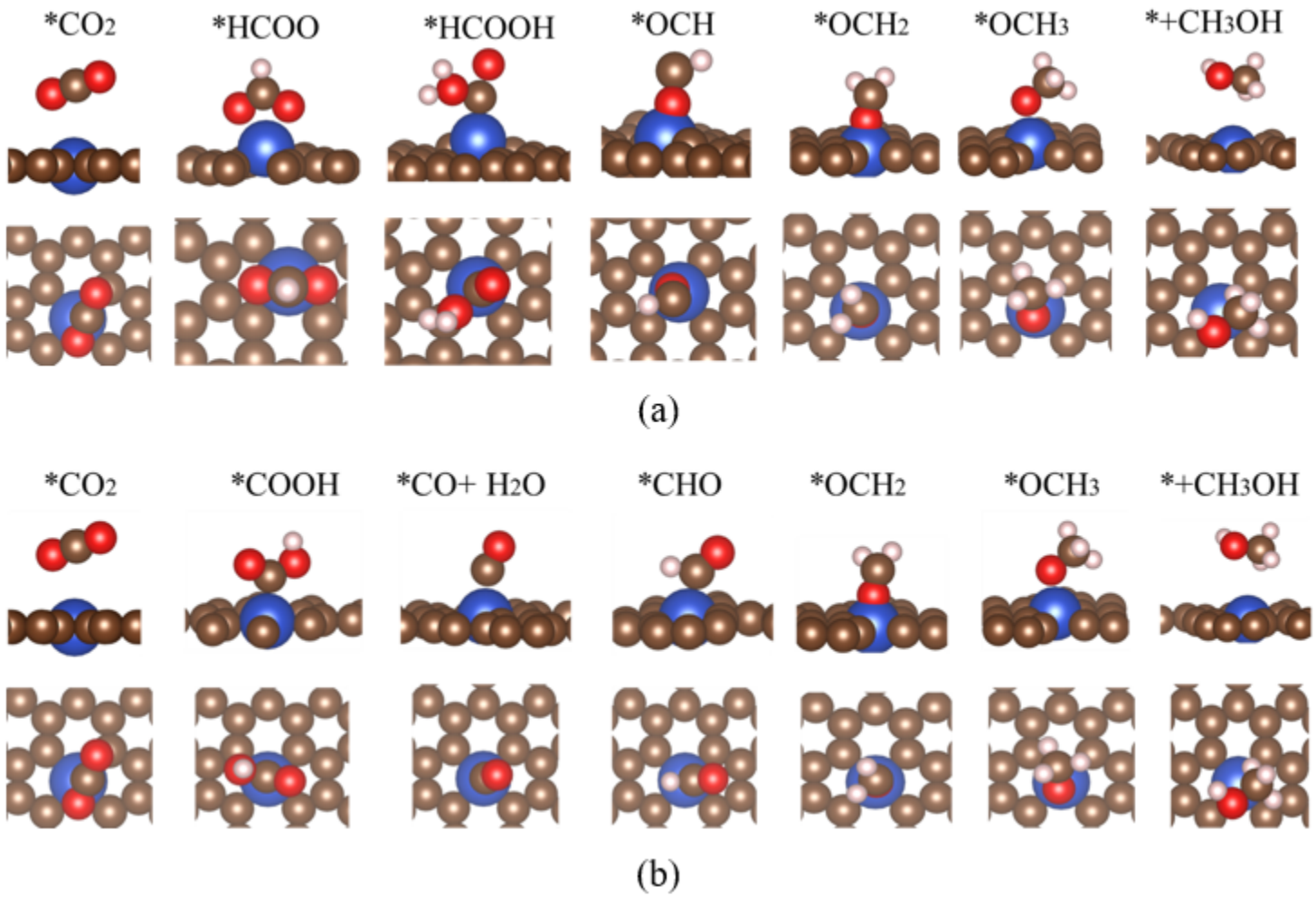

Figure 9

Adsorption structure of intermediate products in two reaction paths for (a) Cu-G4-HCOO-pathway and (b) Cu-G4-COOH-pathway

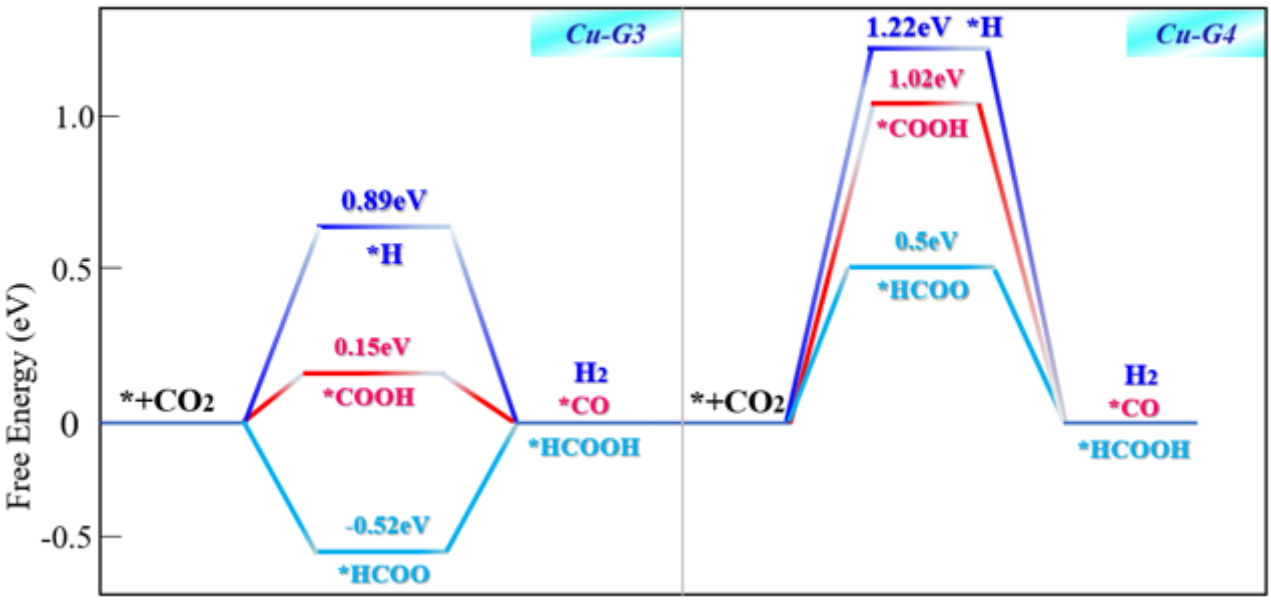

Figure 10

Comparison of free energy of products (H2, *CO,*HCOOH) by first step hydrogenation on two catalysts

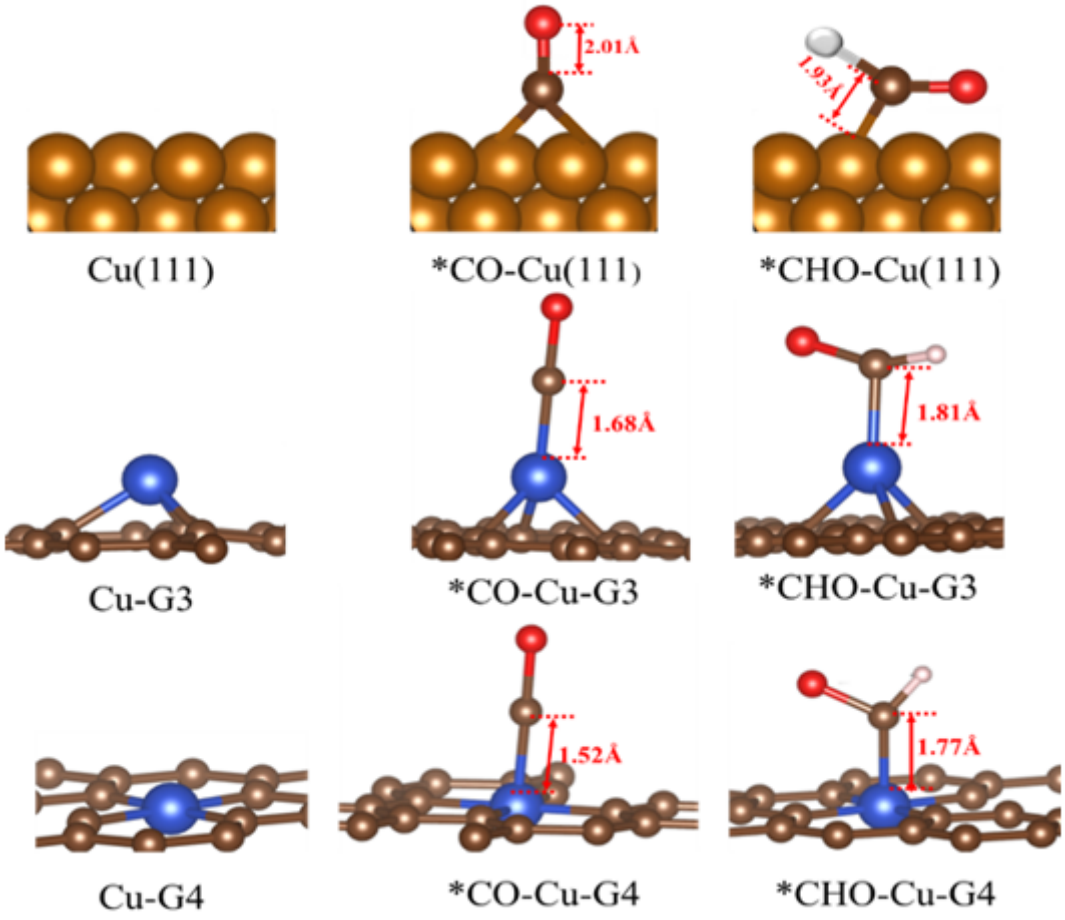

Figure 11

The optimized geometries of the *CO and *CHO species that adsorbed in the catalyst surfaces of Cu (111), Cu-G3, and Cu-G4.

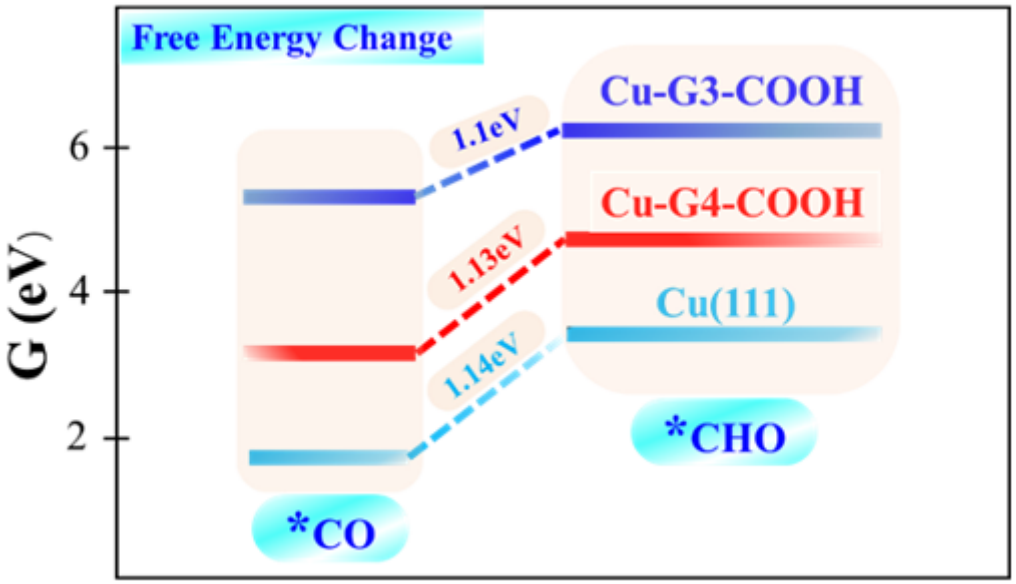

Figure 12

The free energy change from *CO to *CHO on Cu (111), Cu-G3, and Cu-G4 catalysts.

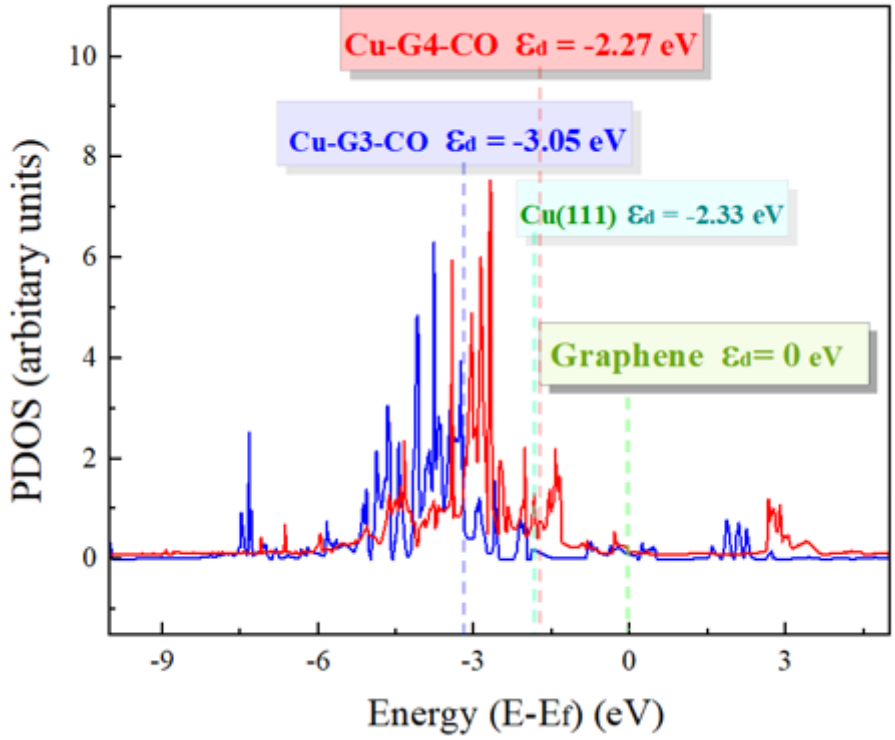

Figure 13

Comparison of the d-band centers of Cu atoms before and after CO adsorption. (The red line denotes Cu-G4/CO, whereas the blue line denotes Cu-G3/CO).

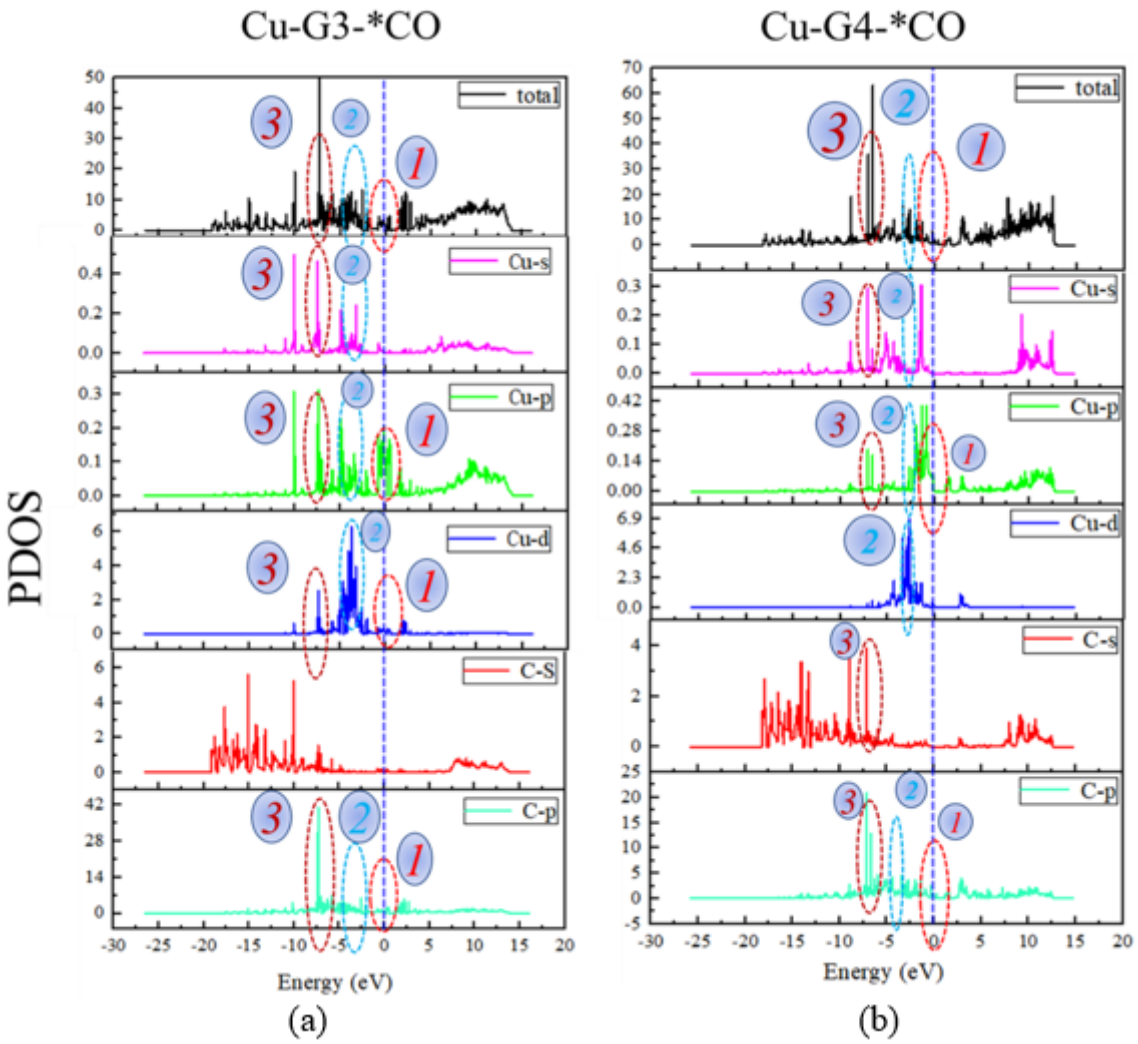

Figure 14

Projected density of states analysis of Cu-G3 and Cu-G4 catalysts after *CO adsorption.

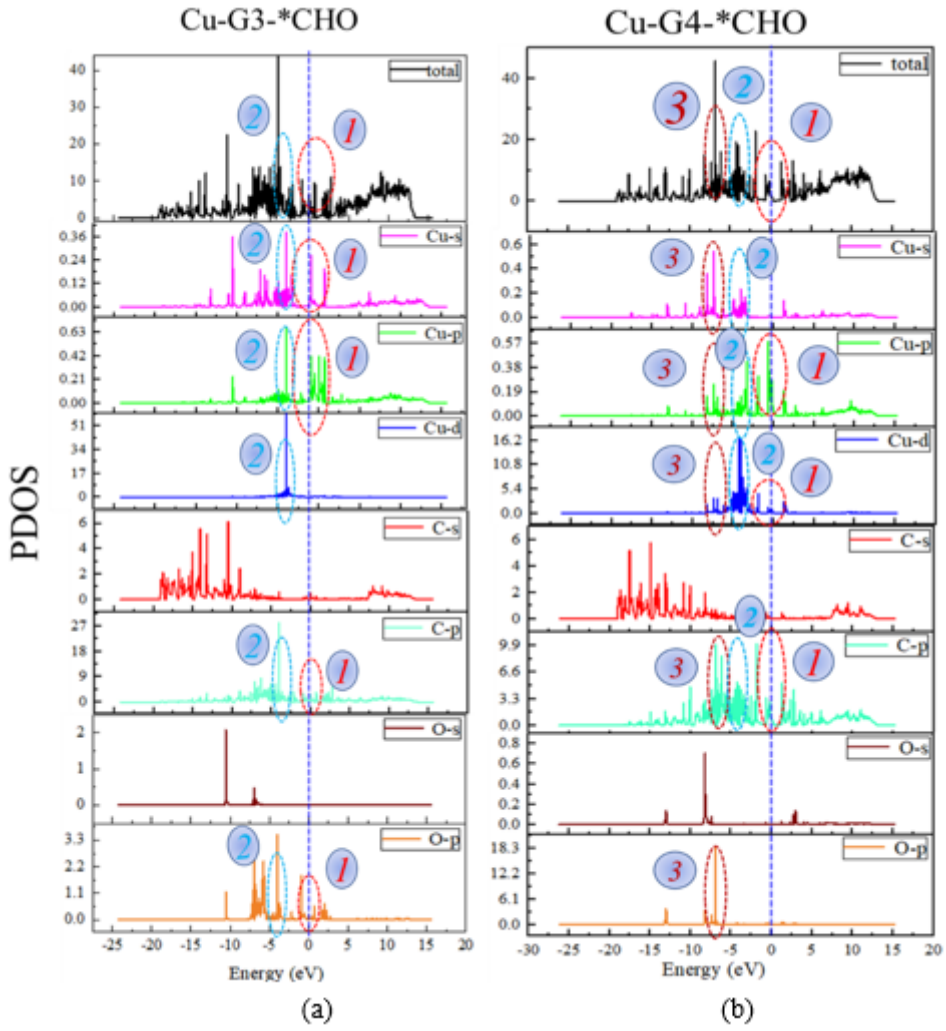

Figure 15

Projected density of states analysis of Cu/G3 ad Cu/G4 after *CHO adsorption.

Supplementary Files

This is a list of supplementary files associated with this preprint. Click to download.

- Supplementaldata.docx